Australasian Physical & Engineering Sciences in Medicine (2019) 42:1025–1032
https://doi.org/10.1007/s13246-019-00801-1

SCIENTIFIC PAPER

Evaluation of dual energy CT and iterative metal artefact reduction (iMAR) for artefact reduction in radiation therapy

P. Lim[1] · **J. Barber**[1,2] · **J. Sykes**[1,2]

Received: 26 June 2019 / Revised: 19 August 2019 / Accepted: 16 September 2019 / Published online: 10 October 2019

Abstract

Metal artefacts pose a common problem in single energy computed tomography (SECT) images used for radiotherapy. Virtual monoenergetic (VME) images constructed with dual energy computed tomography (DECT) scans can be used to reduce beam hardening artefacts. Dual energy metal artefact reduction is compared and combined with iterative metal artefact reduction (iMAR) to determine optimal imaging strategies for patients with metal prostheses. SECT and DECT scans were performed on a Siemens Somatom AS-64 Slice CT scanner. Images were acquired of a modified CIRS pelvis phantom with 6, 12, 20 mm diameter stainless steel rods and VME images reconstructed at 100, 120, 140 and 190 keV. These were post-reconstructed with and without the iMAR algorithm. Artefact reduction was measured using: (1) the change in Hounsfield Unit (HU) with and without metal artefact reduction (MAR) for 4 regions of interest; (2) the total number of artefact pixels, defined as pixels with a difference (between images with metal rod and without) exceeding a threshold; (3) the difference in the mean pixel intensity of the artefact pixels. DECT, SECT + iMAR and DECT + iMAR were compared. Both SECT + iMAR and DECT + iMAR offer successful MAR for phantom simulating unilateral hip prosthesis. DECT gives minimal artefact reduction over iMAR alone. Quantitative metrics are advantageous for MAR analysis but have limitations that leave room for metric development.

Keywords Metal artefact reduction · Dual energy computed tomography · iMAR · Computed tomography · Radiation therapy

Introduction

Conventional single energy computed tomography (SECT) simulations have become the standard of care in the treatment planning of patients undergoing radiotherapy as the ability to convert CT Hounsfield Unit (HU) to tissue electron density is necessary for dose calculations [1]. SECT simulation images provide the foundation for treatment plans and are used for visualising the tumour, contouring structures and calculating the dose to the patient accounting for different tissue types. The accuracy and image quality of the CT images are therefore important in reducing uncertainties that are carried on into patient treatment [2]. A problem in using SECT scans for dose calculations is when image quality is compromised by metal artefacts due to dental implants and metal prostheses [3–5]. Metal artefacts consisting of streaks caused predominantly by beam hardening and photon starvation can compromise delineation of the tumour target and can result in under dosing the target as well as tissue complications from overdosing surrounding normal tissues [6]. Among the metal artefact reduction (MAR) techniques used in CT imaging, dual energy computed tomography (DECT) designed to give the dose of SECT and iterative metal artefact reduction (iMAR) applied retrospectively are potential methods which do not increase the dose burden to the patient [7]. DECT is an adaptation to the conventional technique that acquires two images at different x-ray energies to describe the energy dependent tissue interactions that provide image contrast [8, 9]. Multiple studies have

✉ P. Lim
plim3421@uni.sydney.edu.au

J. Barber
jeffrey.barber@health.nsw.gov.au

J. Sykes
jonathan.sykes@health.nsw.gov.au

[1] School of Physics, University of Sydney, Sydney, Australia

[2] Radiation Oncology, Blacktown Hospital, Sydney West Cancer Network, Sydney, Australia

shown the superiority of using DECT to standard SECT in oncology and radiotherapy applications [6, 7, 10]. Virtual monoenergetic (VME) images, constructed from dual energy scans simulate a monochromic x-ray beam to reduce beam hardening artefacts. iMAR is a postprocessing software implemented on Siemens Syngo platform which combines the normalised metal artefact reduction (NMAR) and frequency split metal artefact reduction algorithms (FSMAR) in an iterative loop [11, 12]. These MAR approaches independently and in combination have the potential to improve tumour delineation and dose calculations where CT numbers have been distorted due to metal artefacts from hip prostheses in prostate and rectal cancers [6, 8, 13–15].

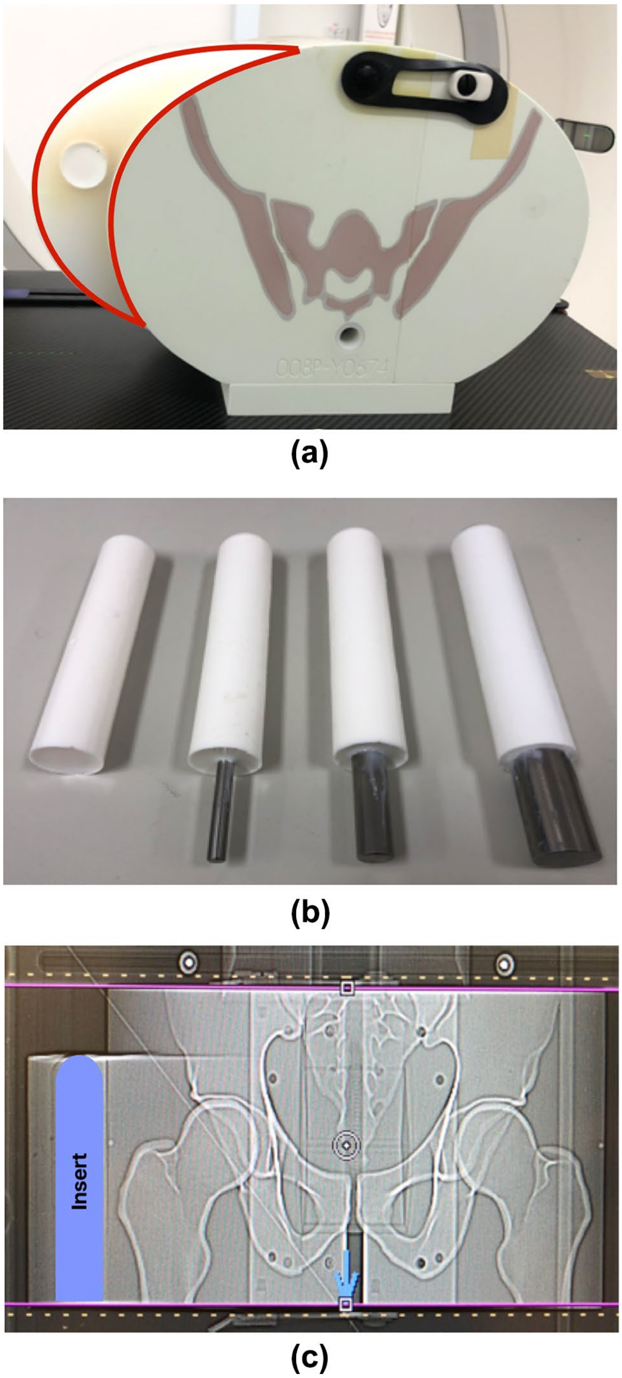

Fig. 1 Phantom simulating unilateral hip prosthesis **a** final phantom setup with attachment (highlighted in red) and polyurethane insert, **b** set of 4 removable polyurethane inserts (no metal, 6 mm, 12 mm and 20 mm 316 stainless steel rods), **c** Topogram of the phantom setup showing the position of the insert (purple) relative to phantom anatomy

Methods

Unilateral hip prosthesis phantom

Hip prostheses typically consists of a metal head tapering to a metal stem to replace the anatomical femur head and the superior portion of the femur bone. A custom built phantom attachment was added onto the anthropomorphic CIRS Dynamic Pelvis Phantom, model 008P (CIRS, Virginia, USA), to simulate the metal artefacts seen in a unilateral hip prosthesis (Fig. 1a). The materials used in the attachment included, Transil silicon rubber and TC808 fast set rigid polyurethane (Barnes, Sydney, AU) and 316 surgical grade stainless steel. Stainless steel rods at 6 mm, 12 mm and 20 mm diameters were used as substitutes for hip prostheses which vary in size, shape and design. The rods represent the metal stem of the prosthesis, with typical cross-sectional dimensions at the distal portion tapering to between 4 and 22 mm, commonly in the same plane as radiotherapy evaluations of the prostate and rectum. The steel rods were imbedded in a polyurethane cast and a set of four polyurethane inserts were constructed (Fig. 1b). The interchange of inserts (no metal, 6, 12 and 20 mm diameter) in the silicon attachment produced a total of four phantom setups used in this experiment.

Computed tomography imaging protocols

SECT and DECT scans were performed on the single source Siemens Somatom Definition AS - 64 slice scanner (Siemens Healthcare, Forchheim, Germany). The CT scan parameters are listed in Table 1. SECT images were acquired with each phantom setup for comparison to standard CT procedures. DECT scans were performed using a dual energy protocol designed to match the standard SECT settings to ensure that the overall imaging dose of the two acquisitions (80 kV and 140 kV) were equivalent to SECT scans. For VME extrapolation, the 80 kV and 140 kV acquisitions were reconstructed to create VME images at 100, 120, 140 and 190 keV. Lastly, iMAR (Siemens Healthcare, Forchheim, Germany) was applied to SECT and DECT acquisitions with the hip prosthesis setting. Images for all the CT acquisitions

Table 1 CT scan parameters for SECT and DECT

CT scan parameter	SECT	DECT	
Tube voltage (kV)	120	80	140
Tube current (mAs)	298	300	71
Acquisition	64 × 0.6 mm	64 × 0.6 mm	64 × 0.6 mm
Slice thickness	2 mm	2 mm	2 mm
Pitch	0.6	0.6	1.2
Reconstruction kernel	B31f	B31f	B31f
Scan protocol	Pelvis_Adult	DE_Abdomen	DE_Abdomen

Includes the parameters for both dual energy acquisitions

and post-processed reconstructions performed on the CT workstation were exported and viewed using DicomBrowser (NeuroInformatics Group, Washington School of Medicine, USA).

Image acquisitions

The different MAR approaches evaluated in this experiment included the CT acquisitions and post-processed reconstructions. 10 image sets were generated for each of the four phantom setups; SECT, SECT reconstructed with iMAR (SECT + iMAR), DECT VME reconstructions at 100, 120, 140 and 190 keV and the four VME reconstructions processed with iMAR (DECT + iMAR). The first phantom setup with the polyurethane insert was used to obtain the non-metal images used as ground truth (GT) for change in metal artefacts seen with 6 mm, 12 mm and 20 mm inserts.

Qualitative analysis

As the first step in MAR analysis, images with fixed window width and window level were placed side by side and compared on visual appearance of artefact. Specific areas of interest for artefacts were close to the metal as well as streaks propagating throughout the phantom body (Fig. 2). The visual reduction from DECT and iMAR approaches were compared relative to the severity of metal artefact observed in SECT. ImageJ (NIH, Bethesda, MD) was used for image processing of the transverse image slice located mid-way through the prostate with rigid registration performed between image sets used to minimise phantom setup variations. Three different metrics were used to quantify MAR (Fig. 3).

Quantitative metric 1: CT HU change in regions of interest (ROI)

The change in CT HU within several specifically placed regions of interest (ROI) has previously been reported to determine CT HU accuracy [3, 15, 16]. ROI were chosen in the phantom image based on artefacts observed from

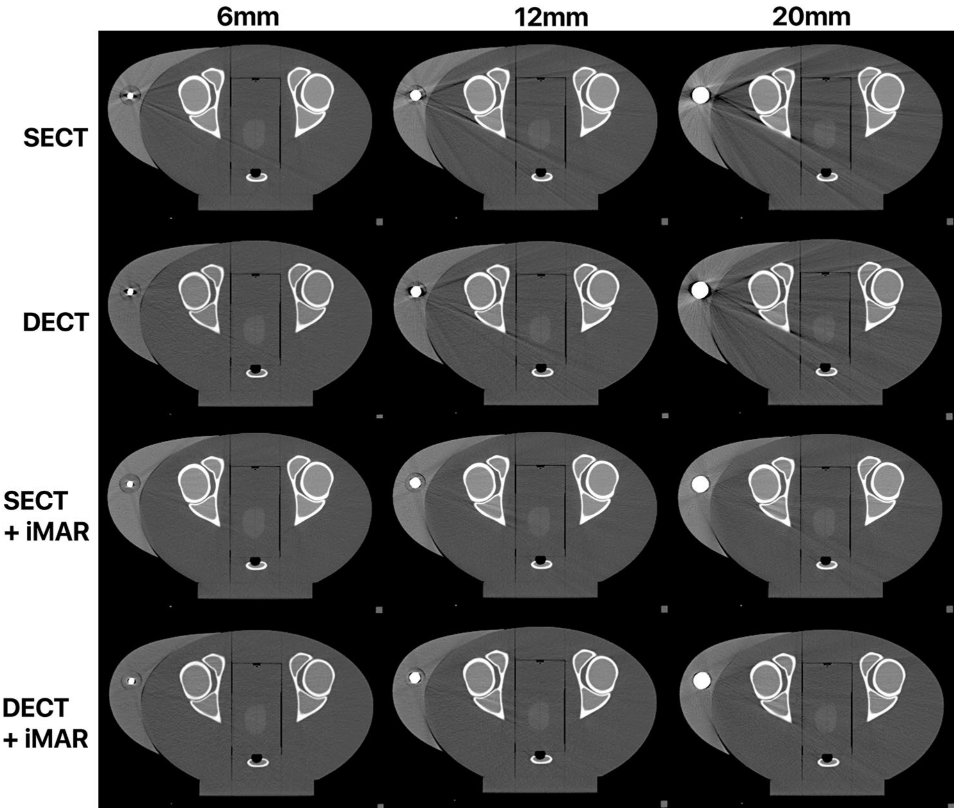

Fig. 2 SECT after applying MAR approaches. Change of metal artefacts from SECT to residual artefacts after DECT, SECT + iMAR and DECT + iMAR approach. The virtual monoenergetic energy corresponding to the optimal DECT images varied between 100 and 120 keV. The virtual monoenergetic energy corresponding to the optimal DECT + iMAR combination varied between 140 and 190 keV

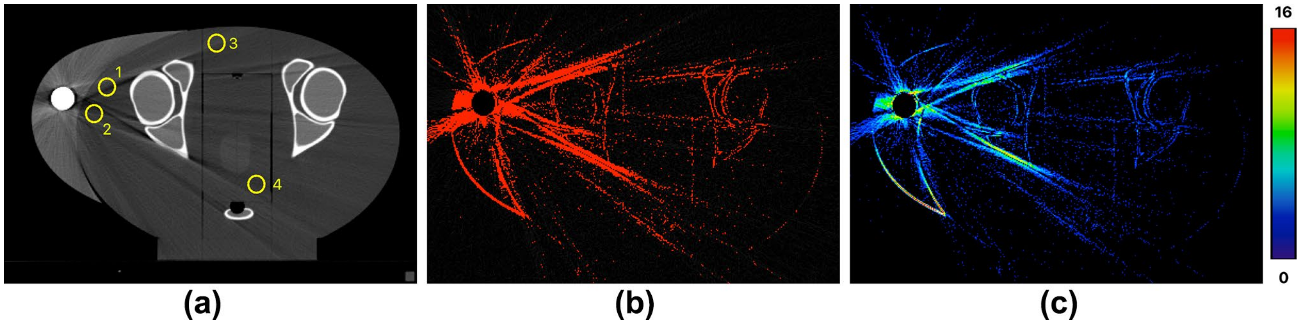

Fig. 3 Quantitative metrics shown for 20 mm phantom setup **a** Metric 1 using ROI on hypodense streaks (ROI 1, 2, 4) and hyperdense steak (ROI 3) **b** Metric 2 artefact image highlighting artefact pixels with 4SD threshold **c** Metric 3 artefact image highlighting the artefact pixel intensity on a 16 colour lookup table

all three stainless steel diameters (Fig. 3a). Two ROI were placed on the main hypodense (dark) streaks near the metal, a third on a hyperdense (bright) streak and a fourth on a hypodense streak adjacent the prostate. The CT HU within the four ROI were measured and the change in HU due to metal artefacts was determined using Eqs. (1) and (2).

$$\Delta HU = \left|HU_{\mathrm{MAR/Metal}} - HU_{\mathrm{No\ MAR/Non\text{-}metal\ GT}}\right| \tag{1}$$

$$\Delta HU_{\mathrm{Total}} = \Delta HU_{\mathrm{ROI1}} + \Delta HU_{\mathrm{ROI2}} + \Delta HU_{\mathrm{ROI3}} + \Delta HU_{\mathrm{ROI4}} \tag{2}$$

For each image set, the change in HU (ΔHU) Eq. (1) was calculated as the absolute change in the HU measured in each ROI compared to the corresponding GT image. The total difference HU ($\Delta HU_{\mathrm{Total}}$) in Eq. (2) was determined by summing the ΔHU across the four ROI and used as the effective artefact magnitude metric. The $\Delta HU_{\mathrm{Total}}$ was measured for the polyurethane insert to look at the effect of MAR on non-metal GT images. The $\Delta HU_{\mathrm{Total}}$ for the three metal inserts was used to look at the effect of MAR. The $\Delta HU_{\mathrm{Total}}$ of SECT images of the metal rods represented the maximum artefacts.

Quantitative metric 2: threshold count for metal artefact pixels

Images were thresholded to highlight metal and artefact regions and quantified with a difference image from GT [17]. Since metal artefacts can appear as light or dark streaks an unsigned (absolute) difference image was generated according to Eq. (3).

$$\text{Artefact image} = \left|\mathrm{Image}_{\mathrm{Metal}} - \mathrm{Image}_{\mathrm{Non\text{-}metal\ GT}}\right| \tag{3}$$

The artefact image referred to in Eq. (3) is the absolute difference between the metal and corresponding non-metal image generated for each image set (SECT, DECT, SECT + iMAR and DECT + IMAR). The stochastic noise contaminating the accurate estimation of metal artefact pixels in the phantom regions was estimated in non-metal GT images across the image sets. The average noise based on the standard deviation (SD) of the mean pixel intensity was 17 ± 2 Gy values. After the high intensity metal insert was segmented out, thresholding at 2SD, 3SD and 4SD was applied to the artefact image to subtract the stochastic noise. The total number of residual pixels in each image set after thresholding were considered artefact pixels and was used to quantify the effect of MAR relative to the number of artefact pixels in SECT (Fig. 3b).

Quantitative metric 3: intensity of metal artefact pixels

It was hypothesized that a higher artefact pixel intensity corresponds to an increased severity or density of the metal artefact streaks. The mean pixel intensity of the remaining artefact pixels selected in metric 2 were determined for each artefact image and used as the artefact magnitude metric (Fig. 3c). To quantify this, the mean pixel intensity was recorded from the mean value of the pixel intensity histogram of the artefact pixels. This was then normalised to the mean pixel intensity of the SECT artefact image.

Results

Qualitative analysis

Figure 2 shows the total artefact seen in SECT decreasing to residual artefact after application of DECT, iMAR and DECT + iMAR. The severity of the metal artefacts increased with larger metal inserts and decreased the degree of MAR seen using DECT. The optimal DECT VME energy for the highest reduction of metal artefacts was different for the three diameters. For the 12 mm and 20 mm phantom setups, the higher VME (120, 140 and 190 keV) caused secondary artefacts around the metal insert where the strong photon starvation was replaced with bright streaks. For the 6 mm phantom setup, the higher VME resulted in minor secondary artefacts and resulted in better MAR. In contrast, iMAR applied to SECT images significantly reduced the metal artefacts without any secondary artefacts. DECT + iMAR achieved the lowest residual artefacts across the three diameters with no visual difference in combinations of 100, 120, 140 and 190 keV as iMAR removed the secondary artefacts caused by high VME energies.

Quantitative metric 1: CT HU change in ROI

The polyurethane insert was used to evaluate the effect of the MAR approaches on the ΔHU_{Total} of GT images. The ΔHU_{Total} effect with iMAR applied to SECT GT and DECT GT images was 0.5–2.2HU. The ΔHU_{Total} difference between DECT GT and SECT GT images was 21.9–32.1HU. The three metal inserts were used to evaluate MAR approaches on the degree of metal artefacts. DECT performed increasingly better at higher energies for hyperdense artefacts (ROI3) by reducing ΔHU (Eq. 1) in SECT to 63%, 37%, 20% and 3% in the 20 mm rod while iMAR reduced the ΔHU to 28%. iMAR performed consistently better for hypodense artefacts (ROI1, ROI2, ROI3) by reducing ΔHU in SECT to an average of 9% compared to the average 21% with DECT. Figure 4 shows the ΔHU_{Total} across the MAR approaches for the three diameter rods.

The optimal DECT VME energy dependent on the diameters of the stainless steel rod varied between 100 and 120 keV. A peak ΔHU_{Total} at 190 keV was caused by a secondary hyperdense streak affecting ROI1 and ROI2. SECT + iMAR and DECT + iMAR approaches had the lowest ΔHU_{Total} to ground truth between 5-10HU which is in the same order of noise in the images. The less than 2HU ΔHU_{Total} between the DECT + iMAR combinations reflect the small visible differences observed in the qualitative analysis. The corresponding images from each MAR approach is shown in Fig. 2. The ΔHU_{Total} for the 6 mm diameter rod were low and reflect the low density artefact seen in the first column of Fig. 2. There is less variation in MAR between DECT and iMAR when the level of artefact is low but the relative trend in MAR is similar to that of the 12 mm and 20 mm diameter rods (Fig. 4).

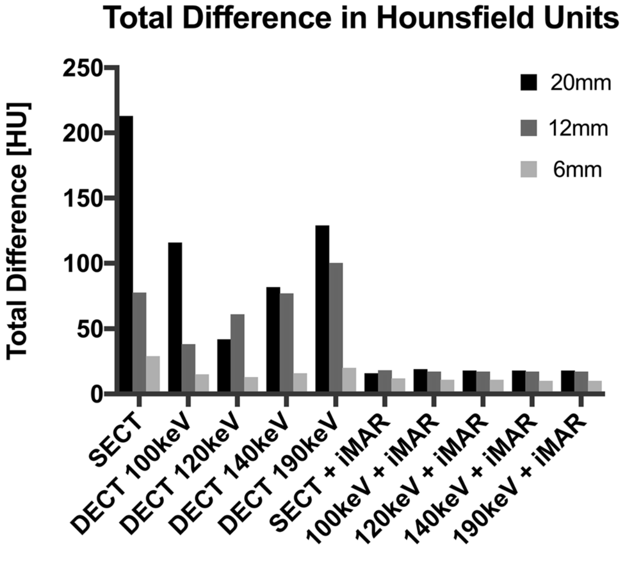

Fig. 4 ΔHU_{Total} (Metric 1) from all MAR approaches for 3 metal rods. Columns represent the ΔHU_{Total} measured across four ROI. SECT is shown in first column for reference to DECT VME and iMAR combinations

Quantitative metric 2: threshold count for metal artefact pixels

The artefact image considered the overall effect of metal artefacts (Eq. 3). A threshold at 4SD of the random noise was found to optimally reduce artefact pixels likely due to random noise while keeping artefact pixels that were clearly metal artefact. In the resulting artefact images for a particular insert, significant differences in HU at regions of very high image gradients led to a fixed number of boundary/edge pixels to be classified as artefact.

For the 20 mm diameter rod, DECT VME images reduced the metal artefacts in SECT to between 85–95%, SECT + iMAR to 58% and DECT + iMAR to 43–49%. SECT + iMAR and DECT + iMAR showed the lowest number of residual artefact pixels. This metric distinguished only small differences in DECT + iMAR images with the lowest number of artefact pixels seen in 190 keV + iMAR (Fig. 5). This trend was seen in 6 mm and 12 mm diameters to a lesser extent.

Quantitative metric 3: intensity of metal artefact pixels

Mean pixel intensity was determined for the artefact pixels highlighted with 4SD in metric 2. Metric 3 had a reduced MAR sensitivity with a maximum of 12% pixel intensity change between MAR for all diameter rods. In Fig. 6 the pixel intensity decreases with the DECT + iMAR combinations for the 6 mm diameter rod. The pixel intensity for the 20 and 12 mm diameters were abnormally high and favoured SECT + iMAR for the lowest artefact intensity. The regions of artefact with high intensity values were predominantly around the edges of the high density bone, metal inserts, phantom attachment and phantom outline.

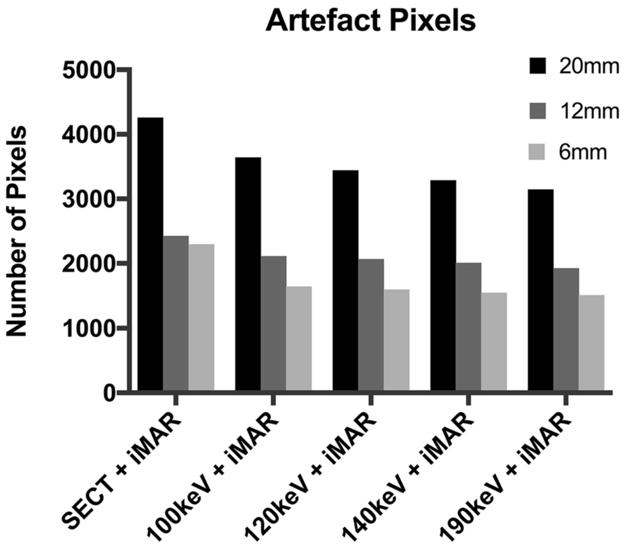

Fig. 5 Artefact pixels (metric 2) highlighted in phantom setups. The DECT + iMAR combinations decreasing number of artefact pixels with higher energy extrapolations. 190 keV + iMAR with the lowest number of artefact pixels in all three diameter rods

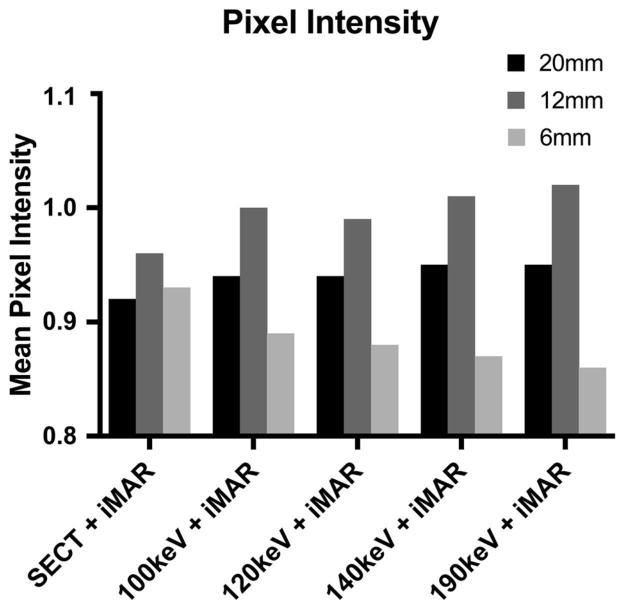

Fig. 6 Mean pixel intensity (metric 3) at 4SD threshold. The mean pixel intensity of SECT + iMAR and DECT + iMAR artefact images were normalised to SECT. Difference in mean pixel intensity was higher for all the MAR approaches in the 12 mm setup

Discussion

The severity of the metal artefacts seen with SECT reflected the high density of steel [14, 15]. The steel rods produced photon starvation and beam hardening artefacts which increased with diameter size. The effect of the variable metal artefacts on the MAR approaches highlight how MAR is highly case specific and dependent on the prosthesis size. 6 mm diameter stainless steel was smaller than the average size of a typical hip prosthesis. 12–20 mm diameters may better represent the typical hip prostheses in adults. Another interpretation of the metal diameters is that hip prostheses are morphologically complicated. Different diameters can represent the tapering of the prosthesis (superior to inferior) and represent different anatomical levels of the metal prosthesis [18].

For DECT alone, higher energy DECT reconstructions were preferred for the small diameter rod while DECT between 100 and 120 keV was optimal for the two larger diameters. This could be because larger diameters have a higher contribution from photon starvation artefacts. The DECT observations are in agreement with the subjective assessment by Wang et al. showing that DECT images above 100 keV marginally improved MAR [18]. Bamberg et al. observed that DECT did not completely but substantially reduced artefacts when compared to the increase of tube voltage and the addition of a tin filter to harden the beam [8]. Due to the restricted selection of virtual monoenergetic energies available, the optimal DECT energy seen in this study could not be compared to the optimal 130 keV as observed by Zhou et al. and other authors [19]. DECT was not the optimal approach for MAR as high VME extrapolations remove beam hardening artefacts without compensating for artefacts caused by photon scattering and photon starvation [20]. Additionally, secondary artefacts were seen around the metal with high energy VME images. Similar secondary artefacts were also observed by Yagi et al. adjacent to a high density cortical bone insert with the use of high energy VME extrapolations [21]. These artefacts would change CT values around the metal and be suboptimal for assessment of targets and regions around the metal. However, in the case of prostate treatments, the secondary artefacts would not have significant impact.

SECT + iMAR was able to significantly reduce artefacts observed in this study. Although projection based MAR algorithms are known for primarily addressing photon starvation artefacts, iMAR was able to suppress most of the metal artefacts (photon starvation and beam hardening). This is likely due to the normalised interpolation algorithm (NMAR) removing photon starvation artefacts and a beam hardening correction algorithm in iMAR separately addressing beam hardening artefacts. The use of iMAR can potentially cause blurring as seen by Bar et al., as the interpolation method used by iMAR removed projection data that were considered metal artefacts [15]. Secondary artefacts from iMAR which appear distant to the metal were observed by Baron et al. However, no additional artefacts from iMAR were seen in this evaluation [22].

The combination of DECT + iMAR was able to achieve the optimal MAR because applying iMAR to DECT removed the secondary artefacts. These observations are aligned with the qualitative results by Bongers et al. where a significant difference was seen with DECT in combination with iMAR [20]. The advantage of the quantitative analysis was to further extract information of the effect of MAR from DECT, SECT + iMAR and DECT + iMAR to give a better estimation of differences. The CT HU values in metric 1 successfully quantified the MAR but only reflected the small differences between DECT + iMAR combinations. The artefact pixels from metric 2 better distinguished the small differences in DECT + iMAR to show 190 keV + iMAR as the best combination with the lowest metal artefacts. Overall, with the small ΔHU_{Total} in DECT + iMAR, it can be assumed any DECT energy combined with iMAR would be acceptable for the entire range of diameters.

In terms of the level of MAR required for radiotherapy, either SECT + iMAR or DECT + iMAR would be acceptable. The level of CT HU accuracy achieved with these approaches can be translated to a less than 1% difference in dose in most regions [15]. As for radiotherapy, the treatment outcome is reliant on dose accuracies of ± 3–4% [23]. A consideration for the practical implementation of DECT on the current CT scanner is that DECT scans must be decided before scanning whereas iMAR can be applied retrospectively as a post-processing technique. In addition, treatment planning systems are typically not well designed for using scans with variable energy and the associated variable CT to ED lookup tables.

Three quantitative metrics were used to quantify MAR through ΔHU, artefact pixels and artefact pixel intensity. The GT differences measured for iMAR are in the order of the differences observed by Axente et al. [24]. Observations with ROI highlighted the effect of the different approaches on metal artefacts stemming from beam hardening verses photon starvation. For the hypodense ROI, iMAR performed better than DECT confirming that projection based MAR methods primarily suppress photon starvation artefacts [25]. For the hyperdense ROI3, DECT performed increasingly better at higher VME energies confirming the inherent ability to minimise beam hardening artefacts. Positioning of ROI took into consideration the hyperdense artefact around the metal, however with ROI placed elsewhere the effect of the secondary artefact could have been missed. The limitations in this metric included the use of ROI which may be limited due to the small coverage. The selection of ROI size and position would affect the results from this metric. A ROI which is too large would allow the non-artefact regions enclosed to average out the CT HU changes in the artefact streaks.

The advantage of metric 2 and 3 was the analysis of MAR throughout the phantom. These metrics relied on the artefact image generated between metal and non-metal images. However, metrics 2 and 3 were contaminated by edge artefacts. This was likely due to the movement of the attachment relative to CIRS phantom which therefore could not be fully corrected by image registration prior to creating a difference image. Only rigid transformations were used to correct for offsets in the phantom setup to minimise the introduction of uncertainties from image processing. Another possibility could be due to differences in the reconstruction algorithm and image registration interpolation that were most pronounced at the edges. While metric 2 was capable of identifying artefact pixels, the same number of pixels around the edges for a particular insert represented a baseline shift in the number of pixels identified as artefact. Only differences in the number of artefact pixels could be quantified and not the absolute number of artefact pixels with MAR. Metric 3 was more sensitive to the contamination of edge artefacts that were predominantly high intensity. These edge artefacts had severe impact on this method for MAR. The segmentation of these artefacts would improve this metric and give a more accurate quantitative representation of MAR.

The limitations in this phantom study include inherent differences between simulated anatomical structures and the larger complexities in patient anatomy. The dual energy analysis on a single source scanner was constrained to fixed VME reconstruction energies. The MAR analysis was performed on a single CT slice in the centre of the phantom where phantom volume could provide a more robust analysis. Additional motion artefacts were not considered for a phantom but would need to be considered for patient scans due to the sequential scanning method used by single source scanner. This limitation is specific to the current scanner and not for the new scanners with dual x-ray tube, fast kV switching or spectral detector technologies. The metrics evaluated in this study may be limited to phantom studies as ground truth images are not available for patients. The effect of prosthesis size on the effect of MAR was evaluated for a simulated hip prosthesis. However, differences in metal composition, positioning and body region could alter the response. Therefore these results are limited to unilateral hip prostheses and may not be translated to dental implants or spinal fixation devices.

Conclusion

In comparison, MAR with DECT did not perform as well as SECT + iMAR or DECT + iMAR. Both SECT + iMAR and DECT + iMAR achieved adequate MAR to be successfully used in radiotherapy for the purpose of accurate structure delineation. This work has covered the imaging perspective and set up the groundwork for further work in analysing the dose errors due to metal artefacts from the different MAR approaches. This work has been based on the assumption that an effect on the CT HU accuracy will affect the resulting dose calculations. From this study, not only was there a need to determine the optimal MAR approach but also the need to determine an appropriate metric to quantitatively analyse the effect of MAR.

Funding No financial funding was provided for this study. An evaluation licence for iMAR was provided by Siemens, in part to perform this study.

Compliance with Ethical Standards

Conflict of interest All author declares that they have no conflict of interest.

Ethics approval This article does not contain any studies with human participants or animals performed by any of the authors.

References

1. Mutic S, Palta JR, Butker EK et al (2003) Quality assurance for computed-tomography simulators and the computed-tomography-simulation process: report of the AAPM Radiation Therapy Committee Task Group No 66. Med Phys 30:2762–2792
2. Bar E, Cisek P, Cwikla J, et al (2014) SOMATOM sessions radiation therapy supplement. Siemens 24
3. Andersson KM, Nowik P, Persliden J et al (2015) Metal artefact reduction in CT imaging of hip prostheses—an evaluation of commercial techniques provided by four vendors. Br J Radiol 88:20140473
4. Hegazy MAA, Eldib ME, Hernandez D et al (2018) Dual-energy-based metal segmentation for metal artifact reduction in dental computed tomography. Med Phys 45:714–724
5. Goo HW, Goo JM (2017) Dual-energy CT: new horizon in medical imaging. Korean J Radiol 18:555–569
6. Giantsoudi D, De Man B, Verburg J et al (2017) Metal artifacts in computed tomography for radiation therapy planning: dosimetric effects and impact of metal artifact reduction. Phys Med Biol 62:R49–R80
7. Van Elmpt W, Landry G, Das M, Verhaegen F (2016) Dual energy CT in radiotherapy: current applications and future outlook. Radiother Oncol 119:137–144
8. Bamberg F, Dierks A, Nikolaou K et al (2011) Metal artifact reduction by dual energy computed tomography using monoenergetic extrapolation. Eur Radiol 21:1424–1429
9. Agrawal MD, Pinho DF, Kulkarni NM et al (2014) Oncologic applications of dual-energy CT in the abdomen. Radiographics 34:589–612
10. Simons D, Kachelrieß M, Schlemmer H-P (2014) Recent developments of dual-energy CT in oncology. Eur Radiol 24:930–939
11. Meyer E, Raupach R, Lell M et al (2010) Normalized metal artifact reduction (NMAR) in computed tomography. Med Phys 37:5482–5493
12. Meyer E, Raupach R, Lell M et al (2012) Frequency split metal artifact reduction (FSMAR) in computed tomography. Med Phys 39:1904–1916
13. Sheen H, Shin H-B, Cho S et al (2017) Feasibility of dual-energy computed tomography in radiation therapy planning. J Korean Phys Soc 71:1056–1063
14. Schwahofer A, Bär E, Kuchenbecker S et al (2015) The application of metal artifact reduction (MAR) in CT scans for radiation oncology by monoenergetic extrapolation with a DECT scanner. Z Med Phys 25:314–325
15. Bär E, Schwahofer A, Kuchenbecker S, Häring P (2015) Improving radiotherapy planning in patients with metallic implants using the iterative metal artifact reduction (iMAR) algorithm. Biomed Phys Eng Express 1:25206
16. Li H, Noel C, Chen H et al (2012) Clinical evaluation of a commercial orthopedic metal artifact reduction tool for CT simulations in radiation therapy. Med Phys 39:7507–7517
17. Morsbach F, Bickelhaupt S, Wanner GA et al (2013) Reduction of metal artifacts from hip prostheses on CT images of the pelvis: value of iterative reconstructions. Radiology 268:237–244
18. Wang F, Xue H, Yang X et al (2014) Reduction of metal artifacts from alloy hip prostheses in computer tomography. J Comput Assist Tomogr 38:828–833
19. Zhou C, Zhao YE, Luo S et al (2011) Monoenergetic imaging of dual-energy CT reduces artifacts from implanted metal orthopedic devices in patients with factures. Acad Radiol 18:1252–1257
20. Bongers MN, Schabel C, Thomas C et al (2015) Comparison and combination of dual-energy- and iterative-based metal artefact reduction on hip prosthesis and dental implants. PLoS ONE 10:1–12
21. Yagi M, Ueguchi T, Koizumi M, et al (2013) Gemstone spectral imaging: determination of CT to ED conversion curves for radiotherapy treatment planning. J Appl Clin Med Phys 14:173–186
22. Baron B, De Marzi L, Pierrat N (2017) Dual energy CT: iterative metal artifact reduction for radiotherapy. Phys Medica 44:29
23. Reft C, Alecu R, Das IJ et al (2003) Dosimetric considerations for patients with HIP prostheses undergoing pelvic irradiation. Report of the AAPM radiation therapy committee task group 63. Med Phys 30:1162–1182
24. Axente M, Paidi A, Von Eyben R et al (2015) Clinical evaluation of the iterative metal artifact reduction algorithm for CT simulation in radiotherapy Clinical evaluation of the iterative metal artifact reduction algorithm for CT simulation in radiotherapy. Med Phys 42:1170–1183
25. Katsura M, Sato J, Akahane M et al (2018) Current and novel techniques for metal artifact reduction at CT: practical guide for radiologists. Radiographics 38(2):450–461